



High-performance PbS quantum dots photodetector based on NiO_x/PbS-EDT heterojunction hole transport layer



Zi Sang ^{a,1}, Cong Zhang ^{a,1}, Xingtian Yin ^{a,*}, Guojiang Qian ^a, Huan Liu ^{b,*}, Wenxiu Que ^a

^a Electronic Materials Research Laboratory, Key Laboratory of the Ministry of Education & International Center for Dielectric Research, Shaanxi Engineering Research Center of Advanced Energy Materials and Devices, School of Electronic Science and Engineering, Xi'an Jiaotong University, Xi'an, Shaanxi 710049, PR China

^b Key Laboratory of Thin Film and Optical Manufacturing Technology, Ministry of Education, Xi'an Technological University, Xi'an, Shaanxi 710021, PR China

ARTICLE INFO

Keywords:

Photodiode
Detectivity
Responsivity
Solution-phase ligand exchange
Solid-state ligand exchange

ABSTRACT

The development of lead sulfide (PbS) colloidal quantum dots (CQDs) with excellent photosensitivity, bandgap tunability and solution processability promises to address the high cost and integration difficulties of commercial III-V semiconductor near-infrared (NIR) detectors. Solution-phase ligand-exchanged (SPLE) PbS-I thin films have received increasing attention due to their high quality and excellent air stability. In recent years, reported PbS-I photodiodes have relied on regular n-i-p structure and solid-state ligand-exchanged (SSLE) PbS-EDT thin films as hole transport layers (HTL). Although these devices exhibit excellent external quantum efficiency (EQE) and responsivity, the large dark current limits the further improvement in detectivity. Considering the advantages of inverted-structure devices in noise suppression, we investigate the effects of three HTLs (NiO_x, PbS-EDT and NiO_x/PbS-EDT heterojunction) on the performance of PbS-I photodiodes. The experimental results show that the device with NiO_x/PbS-EDT as the HTL has lower dark current ($1.6 \times 10^{-3} \text{ mA}\cdot\text{cm}^{-2}$) under -1 V bias compared to the device with single NiO_x or PbS-EDT HTL, which lead to high detectivity ($6.70 \times 10^{11} \text{ Jones}$) and responsivity ($0.487 \text{ A}\cdot\text{W}^{-1}$).

1. Introduction

Near-infrared (NIR) photodetectors enable autonomous driving, spectroscopy, security monitoring and computer vision via light detection and ranging (LiDAR), and hyperspectral imaging technologies [1–3]. The rapid development of a series of emerging fields calls for not only an urgent need to reduce the production cost of photodetectors, but also higher requirements for their detection performance [4–6]. III-V semiconductors (such as InAs and InGaAs) based on epitaxial growth techniques can address some of the prerequisites for high-performance detectors, but the challenges in terms of cost, scalability, inflexibility and integration limit their further application [7–11]. PbS CQDs are expected to become the next generation mainstream NIR materials due to their facile solution processability, size-dependent bandgap (0.6–1.6 eV), high optical absorption coefficient and multiple exciton generation [12–14]. It is worth mentioning that monolithic integration of PbS CQDs with silicon readout integrated circuits (ROICs) has been proved to be a promising method for manufacturing NIR imagers with high-sensitivity and low-cost [15].

In 2014, Bawendi et al. reported a solar cell with PbS-TBAI based on solid-state ligand-exchanged (SSLE) as the photosensitive layer and PbS-EDT as the HTL. The device exhibits a power conversion efficiency (PCE) of 8.55 % with an EQE of more than 50 % at 1000 nm. In this device, the insertion of the PbS-EDT layer not only prevents the flow of electrons from the PbS-TBAI to the anode, but also reduces the surface recombination of photogenerated electrons and holes at the PbS-TBAI/anode interface, which improves the photocurrent harvesting efficiency and the device performance [16]. Compared to SSLE, solution-phase ligand-exchanged (SPLE) overcomes the disadvantages of poor film quality, poor air stability, and poor repeatability, and has shown promising applications in the PbS based photovoltaic field. Sargent et al. demonstrated that a n-i-p structure device with SPLE based PbS-I as the active layer and the PbS-EDT as the HTL can achieve a PCE of 12 % and an EQE of up to 80 %. However, as a photodetector, the reduction of the dark current and the increase of the EQE are equally noteworthy [17]. Optimization of the carrier transport layer in inverted-structured devices has become a reliable strategy for further improving device performance.

* Corresponding authors.

E-mail addresses: xt_yin@mail.xjtu.edu.cn (X. Yin), liuhuan@xatu.edu.cn (H. Liu).

¹ These authors contribute equally to this work

In this paper, we explored the effects of different HTLs (PbS-EDT, NiO_x and NiO_x/PbS -EDT heterojunction) on the device detection performance based on the device with a structure of ITO/HTL/PbS-I/ZnO/Al. Experimental results show that PbS-EDT films can achieve favorable band alignment with the SPLE-based PbS-I CQDs and can block electrons and transport holes to the electrode; NiO_x films based on sol-gel method with a large band gap and high work function can also efficiently collect holes and block electrons [18–20]. However, the dark current level is limited by the large reverse leakage current and is difficult to reduce, both for single-layer NiO_x devices and for single-layer PbS-EDT devices. By constructing the NiO_x/PbS -EDT heterojunction HTL, optimising the devices in terms of interface and energy band structure, we reduce the dark current of PbS photodiode to $1.6 \times 10^{-3} \text{ mA}\cdot\text{cm}^{-2}$ (at -1 V bias), which is 2.0×10^3 times and 93 times lower than NiO_x devices and PbS-EDT devices, respectively. The NiO_x/PbS -EDT heterojunction device show a high detectivity of 6.70×10^{11} Jones and a responsivity of $0.487 \text{ A}\cdot\text{W}^{-1}$.

2. Results and discussion

OA-capped PbS CQDs were synthesized according to the reported method [19]. The first exciton peak of the synthesized PbS CQD in hexane is located at 980 nm, as shown in the absorption spectrum in Figure S1. The transmission electron microscopy (TEM) measurement in Figure S2 was performed on the synthesized CQDs. The diameter distribution of PbS CQDs is presented in Figure S2 as a box plot, showing a

size range of 3.93–4.21 nm and an average diameter of 4.07 nm. The tight bonding of the OA on the surface of the PbS QDs gives it good stability, while maintaining a certain distance between the PbS QDs ensures a good dispersion arrangement in the solution. Uniformly distributed PbS CQDs will ultimately be beneficial for improving the device performance of fabricated photodetectors. The X-ray diffraction (XRD) pattern as shown in Figure S3 is consistent with that reported in other literatures.

We prepared nickel oxide films using the a sol-gel method, whereas PbS-EDT films were prepared using the SSLE, in which insulating OA ligands were exchanged with short-chain EDT ligands [21]. SEM performed on the NiO_x , PbS-EDT and NiO_x/PbS -EDT films to probe into the surface morphology. The surface of the NiO_x film is observed to be rough (Fig. 1(a)), and some significant cracks are observed on the PbS-EDT film (Fig. 1(b)), presumably due to the volume shrinkage during the SSLE [22,23]. Fig. 1(c) shows that the surface of the NiO_x/PbS -EDT heterojunction film is smooth and crack-free. This indicates that the heterojunction construction effectively optimizes the surface morphology of monolayer HTLs, providing a basis for reducing the leakage current. The optical transmission spectra of NiO_x , PbS-EDT and NiO_x/PbS -EDT films are shown in Fig. 1(d). The transparency of NiO_x films exceeds 95 % across the visible and near-infrared spectral ranges. Following the deposition of PbS-EDT films, the transmission is significantly reduced. PbS-EDT and NiO_x/PbS -EDT films retain nearly identical transmission spectra, with minor fluctuations.

The composition of the prepared NiO_x film was investigated using

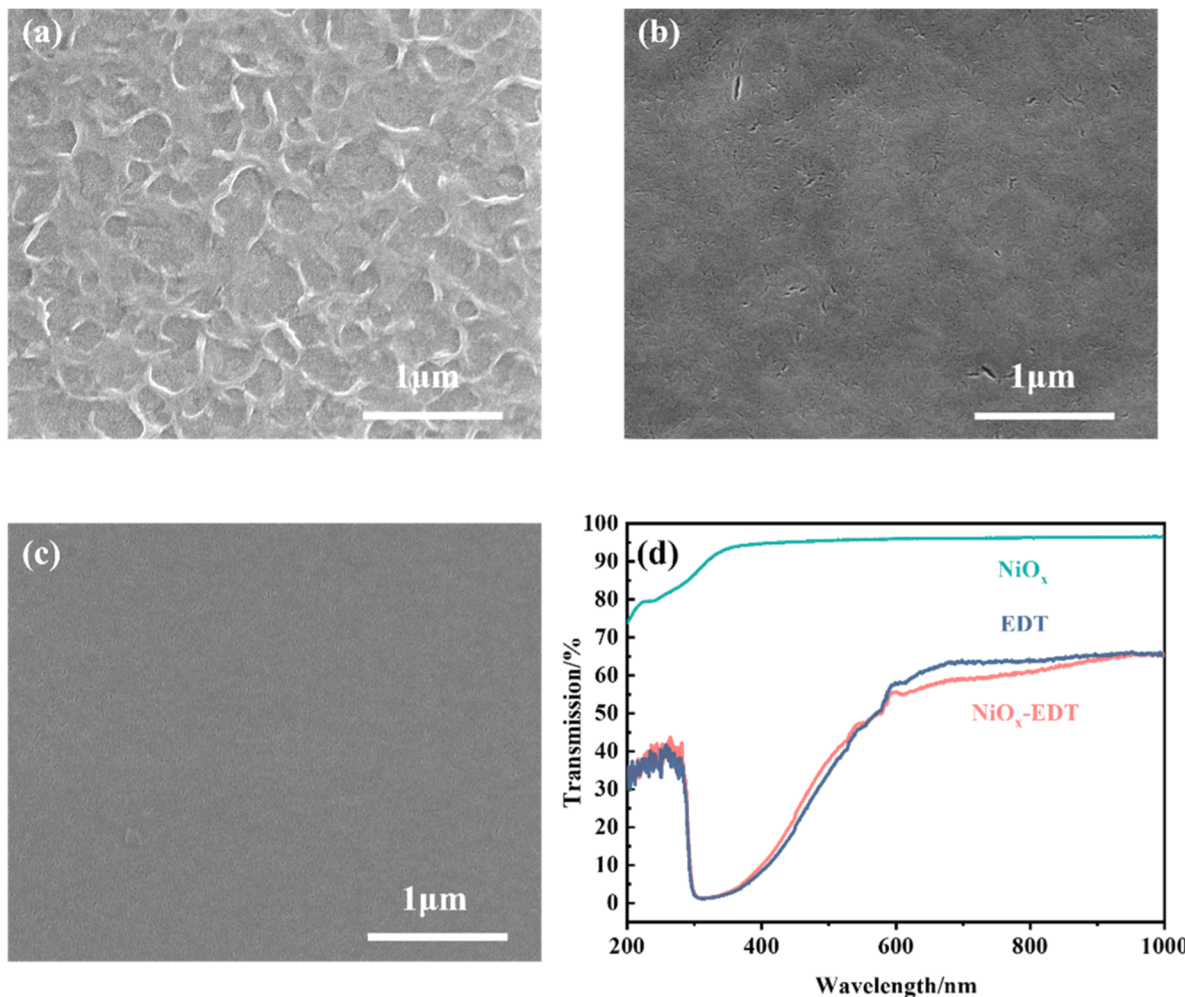


Fig. 1. Top-view SEM images of (a) the NiO_x film (b) the PbS-EDT film and (c) the NiO_x/PbS -EDT film. (d) Transmission spectra of NiO_x , PbS-EDT and NiO_x/PbS -EDT films.

the X-ray photoelectron spectroscopy (XPS). Fig. 2(a) and (b) show XPS spectra of Ni 2p and O 1 s core level. The broad peak at 861.2 eV in the Ni 2p spectrum is ascribed to the shake-up process of NiO_x . The XPS spectra comprise several components, including NiO (Ni 2p at 854.2 eV and O 1 s at 529.5 eV), Ni_2O_3 (Ni 2p at 855.8 eV and O 1 s at 531.3 eV), and NiOOH (Ni 2p at 857.2 eV and O 1 s at 532.9 eV). According to XPS, it can be seen the presence of Ni^{3+} in the NiO_x film, which leads to defects and makes it have the function of hole transport [24,25].

SPLE-based PbS-I devices exhibit a PCE of up to 14 % in the photovoltaic field. Compared to SSLE-based films, SPLE-based films have significant advantages in film quality, carrier mobility, air stability and repeatability, making them increasingly used in the active layer of photodiodes. We replaced the long-chain OA ligands of PbS CQDs with iodine through a typical SPLE process and dissolved them in a mixed amine solution at a concentration of 300 mg/ml. As shown in Fig. 3(a), the surface of the PbS-I film is smooth and no cracks or holes are found even at 80000 magnification. Fig. 3(b) shows that the first exciton absorption peak of the PbS-I film is located at 995 nm. The Fourier transform infrared spectroscopy (Fig. 3(c)) demonstrated the adequacy of ligand exchange: the PbS QDs-OA film exhibits strong bands due to asymmetrical and symmetrical stretching vibrations of C–H (from the alkyl chain of OA ligand) at 2917 and 2849 cm⁻¹ and COO⁻ at 1542 and 1404 cm⁻¹, but the above vibrations are not observed in the PbS-I film, which indicates the SPLE process can effectively remove OA ligands [26]. Fig. 3(d) illustrates that the ZnO film prepared by spin coating contains a small amount of pin holes.

The schematic diagram of the device structure is shown in Fig. 4(a). From the bottom to the top, there are the glass substrate, the indium tin oxide (ITO) transparency electrode, the $\text{NiO}_x/\text{PbS-EDT}$ HTL, the halide passivated PbS CQDs absorber layer, the ZnO ETL, and the Al electrode in sequence. Fig. 4(b) shows a cross-sectional-view SEM image of the as-fabricated $\text{NiO}_x/\text{PbS-EDT}$ based PbS QD photodetector. The thickness of each functional layer is sequentially ~20 nm (NiO_x), 300 nm (PbS-I), 20 nm (ZnO), and 200 nm (Al electrode). The corresponding band structure diagram is given in Fig. 4(c). Ultraviolet photoelectron spectroscopy (UPS) measurements were conducted on the NiO_x layer. As shown in Figure S4, the Fermi level of the NiO_x layer is located at -4.97 eV, and the maximum valence band is located at -5.77 eV. By combining its optical band gap of 3.84 eV, the minimum conduction band is located at -1.93 eV. The band energy positions of the ZnO, the PbS-I, and the PbS-EDT layers were extracted from the literature [27]. The NiO_x interlayer has a much higher minimum conduction band energy than that of the PbS-EDT layer, which could block the electrons at the interface of the back contact, thus improving the photodetector performance [28].

The I–V curves of the device under dark and NIR incident light

(@1064 nm, 90.6 mW) are shown in Fig. 5(a). At a bias voltage of 0 V (self-powered mode), the NiO_x device, the PbS-EDT device and the $\text{NiO}_x/\text{PbS-EDT}$ device exhibit photocurrent densities of 2.4, 6.6 and 27.2 mA·cm⁻² respectively as well as similar dark current densities (about 10^{-3} mA·cm⁻²). When the reverse bias voltage is -1 V, the photocurrent densities of the three devices are 116.8, 7.9 and 44.3 mA·cm⁻², respectively; and the dark current densities are 3.3, 0.15 and 1.6×10^{-3} mA·cm⁻² in the sequence. Compared to the NiO_x HTL, the PbS-EDT HTL exhibits better reverse leakage current suppression, effectively reducing the dark current densities by an order of magnitude. The construction of the $\text{NiO}_x/\text{PbS-EDT}$ heterojunction further optimizes the reverse leakage current of the device. The dark current is further reduced by two orders of magnitude compared with the PbS-EDT device, probably due to the significantly optimized surface morphology of the $\text{NiO}_x/\text{PbS-EDT}$ heterojunction. As an important factor affecting the detectivity of CQDs photodiodes, dark current reduction has been a focus of interest for researchers. Fig. 5(b) and (c) show the variation of the responsivity and detectivity of the three devices depending on applied voltage. Thanks to the significantly reduced dark current, the $\text{NiO}_x/\text{PbS-EDT}$ heterojunction device exhibits a detectivity of up to 10^{11} jones in the bias voltage range 0 V to -1 V, significantly higher than those of the NiO_x device and the PbS-EDT device. The detectivity and responsivity of the three devices under 0 V and -1 V are shown in Table 1.

Fig. 6(a) and (b) show the variation curve of responsivity and detectivity of the three devices with varying optical intensity. The responsivity and detectivity increase with the attenuation of the incident light power. This phenomenon is ubiquitous in CQDs-based photodetectors: On the one hand, the enhanced inverse electric field induced by the high optical intensity promotes the recombination of photo-generated carriers and reduces the gain of the device. On the other hand, at high luminosity power, the sub-band gap states are populated by a massive photo-energized carrier, leading to an enhancement of the quasi-Fermi level. This reduces the ability of the trapped state to trap charge carriers. Compared to the two single-layer HTL devices, the heterojunction devices exhibit higher detectivity and responsivity under different incident light powers. When the incident light power is 1.1×10^{-4} W·cm⁻², the detectivity of the heterojunction device is 5.43×10^{12} Jones. Table S1 summarizes the device architectures and detection performance of representative PbS CQD photodiodes reported in recent years. It can be seen that, compared with both regular and inverted architectures, the device reported in this work—featuring a $\text{NiO}_x/\text{PbS-EDT}$ heterojunction as the hole transport layer—exhibits competitive detection performance.

Fig. 7 shows transient response curves of three devices (@1064 nm, 90.6 mW). It can be seen that the sensitized device can rapidly rise/

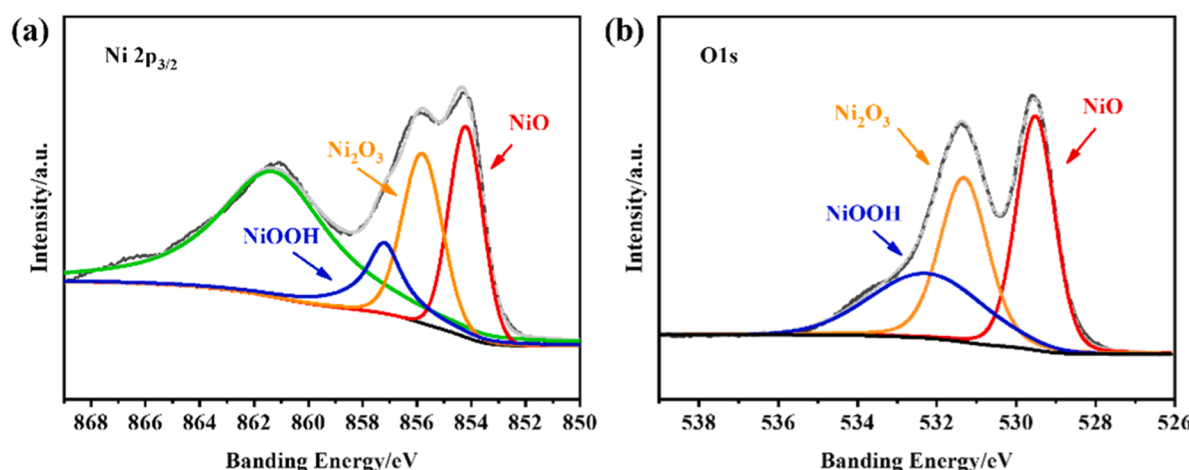


Fig. 2. High resolution (a) Ni 2p and (b) O 1 s XPS acquisition for the NiO_x film.

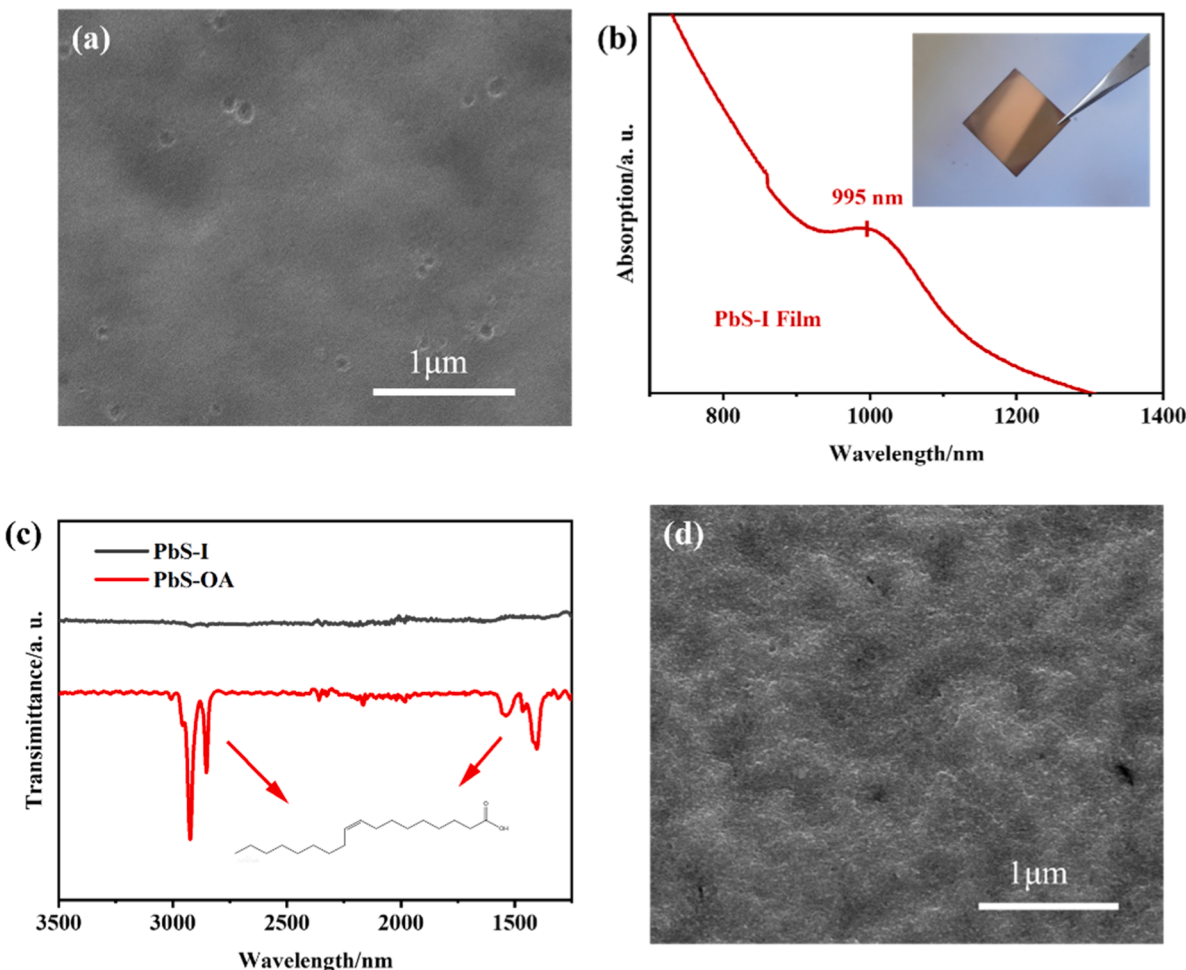


Fig. 3. (a) The top-view SEM image of the PbS-I film and (b) the absorption spectrum of the PbS-I film. (c) The fourier transform infrared spectroscopy of PbS-OA and PbS-I films. (d) The top-view SEM image of the ZnO film.

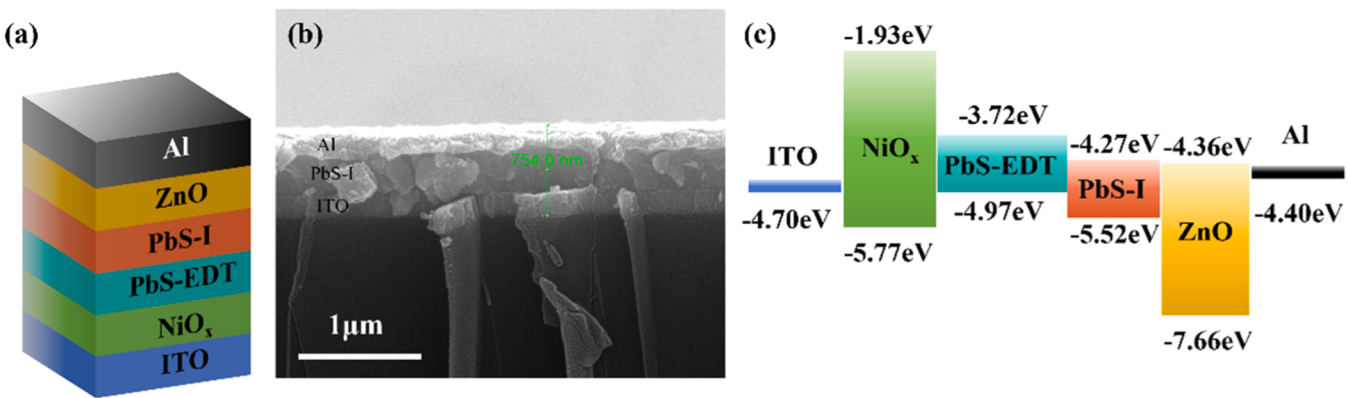


Fig. 4. The (a) schematic device structure (b) cross-sectional SEM image and (c) band diagram of the $\text{NiO}_x/\text{PbS-EDT}$ based photodetector.

decay to a stable value after the incident light is irradiated/removed, both NiO_x , PbS-EDT and $\text{NiO}_x/\text{PbS-EDT}$ based devices exhibit a rise time lower than 60 μs and a fall time lower than 20 μs . Further switch repeatability test is shown in Fig. 8(a), (b) and (c), It can be seen that devices with different HTL exhibits good on-off repeatability under 1 Hz illumination, which is a benefit from the stable chemical properties and carrier transport mechanism of the NiO_x and PbS-EDT HTLs.

3. Conclusion

In summary, we fabricated a 1064 nm-operating CQD-based photodetector. By constructing $\text{NiO}_x/\text{PbS-EDT}$ heterojunctions and optimising the interface between the functional layers to enhance band alignment and block the electrons at the surface of the back contact, thus improving the photodetector performance. The $\text{NiO}_x/\text{PbS-EDT}$ based device achieves a low dark current ($1.6 \times 10^{-3} \text{ mA}\cdot\text{cm}^{-2}$ at -1 V bias voltage) and high detectivity ($6.70 \times 10^{11} \text{ Jones}$ at -1 V bias voltage),

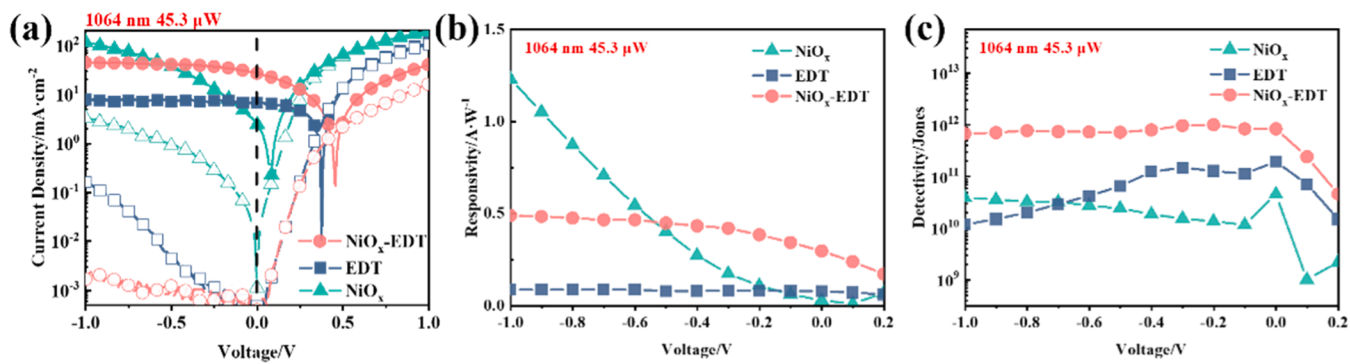


Fig. 5. (a) I–V curves under dark and NIR incident light (@1064 nm, 90.6 mW·cm⁻²) of the NiO_x/PbS-EDT heterojunction HTL device and the NiO_x, PbS-EDT single-layer HTL device. (Solid symbols represent photocurrent data, while hollow symbols represent dark current data.) The (b) detectivity and (c) responsivity of the three devices with different voltage.

Table 1

Comparison of the detectivity and responsivity of the three devices.

	Responsivity (A·W ⁻¹)		Detectivity (Jones)	
	0 V	-1V	0 V	-1V
NiO _x	0.027	1.230	4.49×10^{10}	3.82×10^{10}
EDT	0.076	0.084	1.93×10^{11}	1.16×10^{10}
NiO _x -EDT	0.295	0.487	8.29×10^{11}	6.70×10^{11}

8.29×10^{11} Jones at 0 V bias voltage) and responsivity ($0.487 \text{ A}\cdot\text{W}^{-1}$ at -1 V bias voltage, $0.295 \text{ A}\cdot\text{W}^{-1}$ at 0 V bias voltage), it also exhibits good transient response and on-off repeatability. This heterojunction design provides a simple idea for building photodiodes with better performance.

4. Experimental section

4.1. Preparation of PbS QDs

0.4464 g of lead oxide (PbO), 1.5 ml of oleic acid (OA) and 10 ml of octadecene (ODE) were added to a three-necked flask. The reaction system was warmed up to 95 °C and vacuumed for two hours. Keep the reaction system in nitrogen environment for 15 min and heat up to 120 °C. When the temperature was stabilized, the reaction system was rapidly injected with a mixture of 0.21 ml of bis(trimethylsilyl)sulfide (HMS) and 10 ml of ODE. The heating was stopped immediately and the solution in the three-necked flask was transferred to a dispensing funnel after an ice-water bath to room temperature and the reaction was terminated by the addition of 25 ml of acetone. Then 5 ml of toluene and 15 ml of strong polar solvent methanol were added in the dissolution of quantum dots, which was left to precipitate in layers. Take the lower layer of black

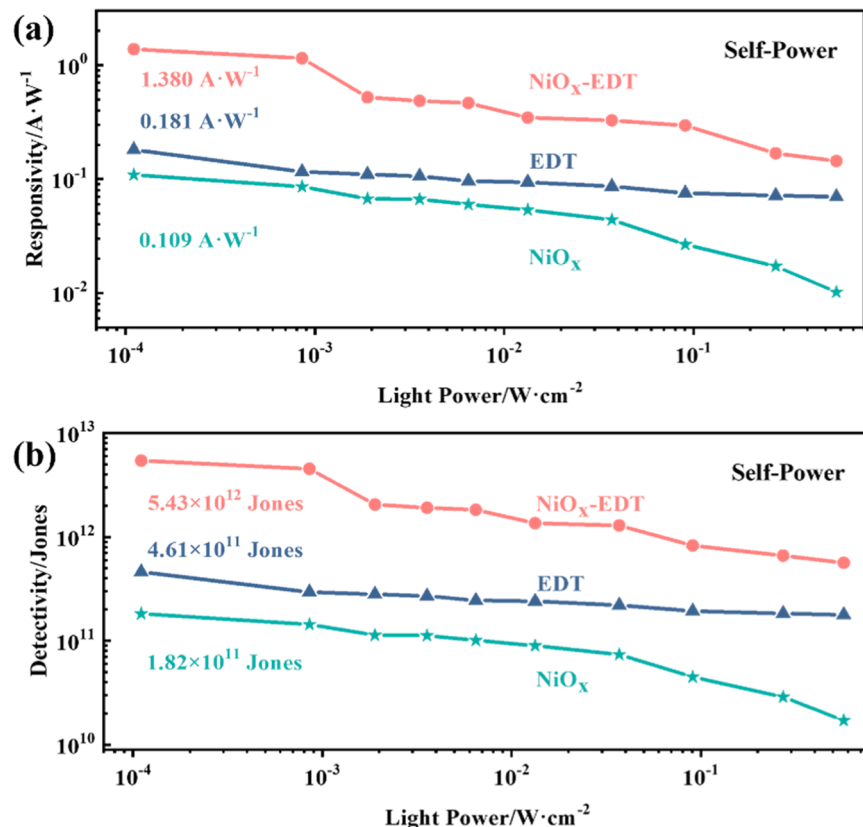


Fig. 6. (a) The responsivity and (b) the detectivity of three devices with different incident light power.

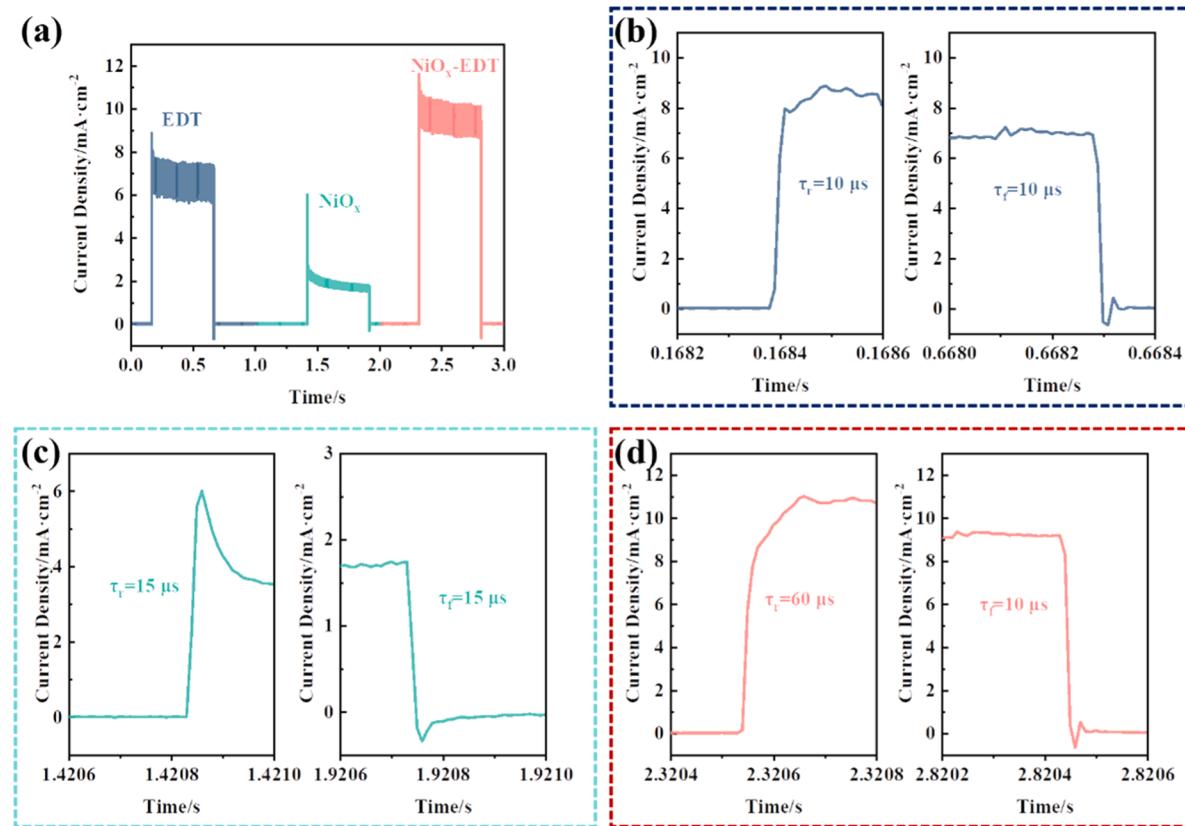


Fig. 7. (a) Transient response curves of the PbS-EDT based device, the NiO_x based device and the NiO_x/PbS-EDT based device (@1064 nm, 90.6 mW). (b) Rise time and fall time of PbS-EDT device. (c) Rise time and fall time of NiO_x device. (d) Rise time and fall time of NiO_x/PbS-EDT device.

liquid and add excess acetone, shaking, centrifugation, pour off the supernatant, add 2 ml of toluene to dissolve the black solid, repeat the acetone wash twice. Finally, the centrifuged PbS QDs were placed in a vacuum oven for 1 h, then removed and stored in a glove box.

4.2. Solution-phase ligand exchange process

The 0.1 M lead iodide (PbI₂) and 0.04 M ammonium acetate (NH₄Ac) were dissolved in a solution of dimethylformamide (DMF) and stirred for one hour. Subsequently, an equal volume of n-hexane solution containing quantum dots (QDs) at a concentration of 10 mg/ml was added to the PbI₂ DMF solution and vigorously stirred until complete transfer of all PbS QDs into the DMF phase was achieved. The resulting black lower layer was separated using a separating funnel, followed by shock cleaning with n-hexane, and cleaning steps were repeated twice. To precipitate the quantum dots, an equal volume of toluene was introduced as an antisolvent. The obtained QD solid was then subjected to centrifugation and vacuum dried for two hours, yielding dry powder of PbS-I QDs.

4.3. Solid-state ligand exchange process

The PbS-OA ink was obtained by dissolving the OA-capped quantum dots in a 50 mg/ml n-octane solution, followed by filtration. Subsequently, the PbS-OA ink spin-coating process was performed on the substrate at 3000 rpm for 20 s. Afterwards, the sample was covered with an EDT solution (0.02 % acetonitrile by volume) and held for 30 s to ensure complete ligand exchange. Finally, two rinse-spin steps were carried out using acetonitrile.

4.4. Preparation of NiO_x films

To prepare the NiO_x precursor solution, 99.5 mg of NiAc was added to a mixture of 4 ml ethanol and 24.5 mg ethanolamine, followed by stirring at 70 °C for 4 h. The NiO_x solution was spin-coated onto the substrate in an ambient air environment, with the spin-coating parameters set at 2500 rpm for 60 s. Subsequently, the film underwent stepwise annealing: first at 100 °C for 2 min, then raised to 145 °C for another 2 min, further increased to 190 °C for an additional period of 2 min, annealed at 235 °C for another duration of 2 min, and finally annealed at a temperature of 275 °C for 45 min. The hot plate was turned off and the film was allowed to cool naturally until it reached room temperature, resulting in the formation of a light green NiO_x film.

4.5. Preparation of ZnO film

2.3 g of ZnAc₂·2H₂O was dissolved in 125 ml of methanol and stirred at 60 °C in a water bath until it was dissolved. Separately, 1.48 g of KOH was dissolved in 65 ml of methanol and added dropwise to the ZnAc₂ solution. The resulting mixture was stirred vigorously at 60 °C for 2.5 h, then cooled. The colloidal solution was centrifuged to obtain the precipitate. Afterwards, add methanol and sonicate for 5 min. Repeat the cleaning process twice to obtain ZnO precipitate. Disperse the precipitate in a methanol chloroform (1:1, vol%) solution to form a 5 mg/ml colourless and transparent ZnO solution. Store the solution in a refrigerator at low temperature. To obtain the electron transport layer, spin coat the appropriate amount of solution at 4000 rpm for 30 s onto the light absorption layer, and anneal at 70 °C for 30 min.

4.6. Device fabrication

The device was fabricated on a glass substrate covered with striped

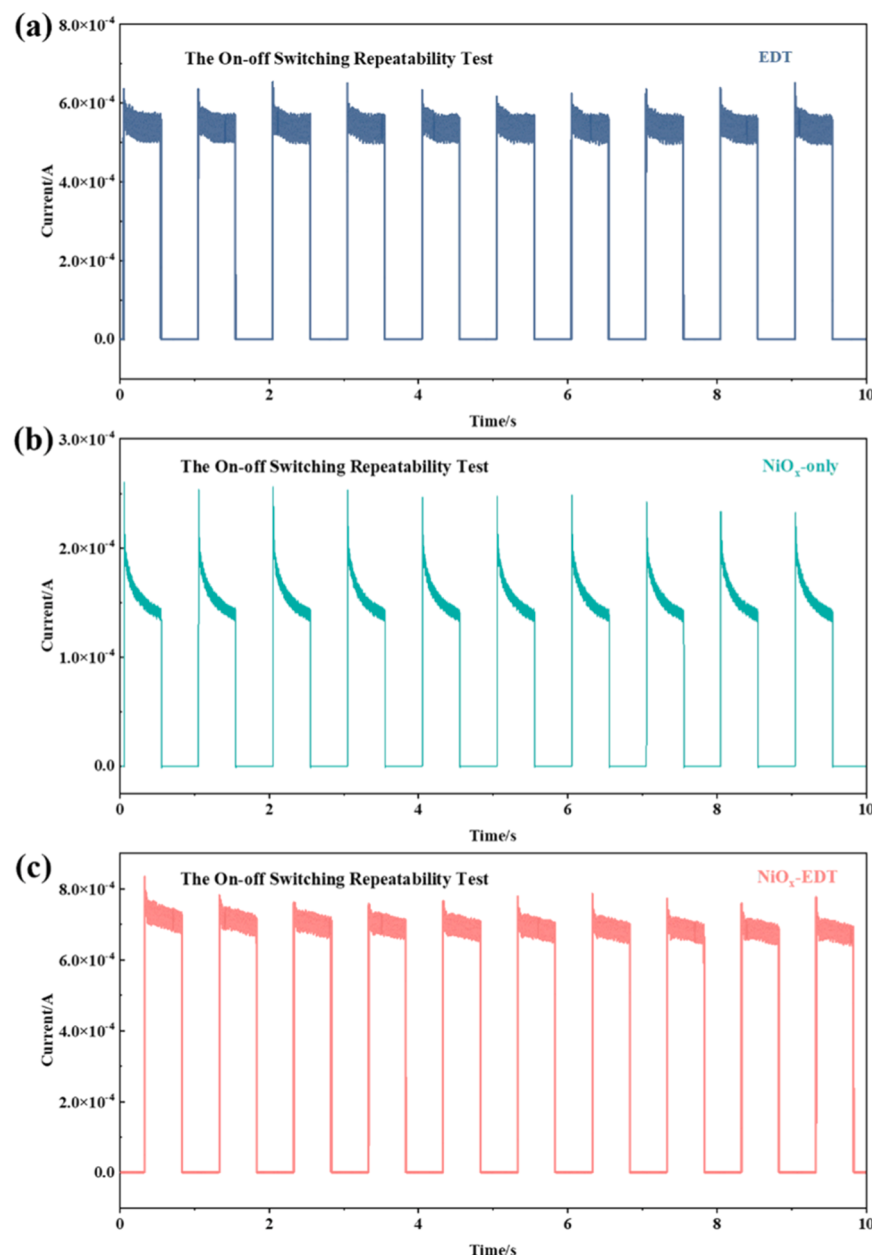


Fig. 8. On-off switching repeatability tests of the (a) PbS-EDT (b) NiO_x (c) NiO_x/PbS-EDT based photodetector.

ITO electrodes. Firstly, the HTL NiO_x was spin-coated on the pre-cleaned glass substrate according to the above recipe, followed by spin-coating the PbS-EDT layer. PbS-I powder was dissolved in a mixture of butamine/pentamine/hexamine (10:3:2, vol%) at a concentration of 300 mg/ml. The PbS-I ink was spin-coated at 2500 rpm for 60 s, 100 °C annealing 30 min to obtain the absorption layer. Then ZnO was spin-coated as the ETL and finally Al was evaporated as the electrode.

4.7. Characterization

The crystal properties were characterized by D/max-2400 XRD spectrometer (Rigaku, Japan) using Cu Ka radiation. The absorption spectra of the samples were determined by PE Lambda950 UV-vis-NIR spectrometer. The surface morphology of films were obtained by the SEM (quanta250 FEG, FEI Inc, Hong Kong). The microstructure of the prepared quantum dots was observed by transmission electron microscopy (TEM, Talos F200X, Thermo Fisher Scientific Inc., USA).

4.8. Statistical analysis

The sample size (n) was described within the captions of the corresponding figures. The Origin Pro Software was used for data processing and analysis.

CRediT authorship contribution statement

Zi Sang: Writing – original draft, Formal analysis, Data curation, Conceptualization. **Cong Zhang:** Writing – review & editing, Investigation. **Huan Liu:** Supervision, Conceptualization. **Wenxiu Que:** Writing – review & editing, Supervision. **Xingtian Yin:** Writing – review & editing, Resources, Funding acquisition, Conceptualization. **Guojiang Qian:** Project administration, Conceptualization.

Declaration of Competing Interest

The authors declare that they have no known competing financial

interests or personal relationships that could have appeared to influence the work reported in this paper.

Acknowledgments

This work was funded by the Natural Science Foundation of Shaanxi Province (2024JC-ZDXM-38) and the Fundamental Research Funds for the Central Universities (xzy 012022090).

Appendix A. Supporting information

Supplementary data associated with this article can be found in the online version at [doi:10.1016/j.jallcom.2025.181671](https://doi.org/10.1016/j.jallcom.2025.181671).

References

- [1] L.I.U. Wu, Y.E. Zhenhua, Status and trends of foreign infrared photodetectors, *Laser Infrared* 41 (4) (2011) 365–370.
- [2] F.P.G. de Arquer, D.V. Talapin, V.I. Klimov, Y. Arakawa, M. Bayer, E.H. Sargent, Semiconductor quantum dots: technological progress and future challenges, *Science* 373 (6555) (2021) 640–654.
- [3] S.-H. Kim, D. Lee, S. Moon, J.-H. Choi, D. Kim, J. Kim, S.-W. Baek, Sulfurized colloidal quantum dot/tungsten disulfide multi-dimensional heterojunction for an efficient self-powered visible-to-SWIR photodetector, *Adv. Funct. Mater.* 33 (43) (2023) 2303778.
- [4] A. De Iacovo, C. Venettacci, L. Colace, L. Scoppi, S. Foglia, PbS colloidal quantum dot photodetectors operating in the near infrared, *Sci. Rep.* 6 (2016) 37913.
- [5] C. Zhang, X. Yin, G. Qian, G. Chen, S. Iqbal, W. Que, Paper-based lead sulfide quantum dot heterojunction photodetectors, *Adv. Mater. Technol.* 9 (3) (2024) 2301723.
- [6] A. Liu, J. Zhao, Q. Tan, P. Yang, Y. Liu, Q. Wang, Enhanced optoelectronic characteristics of MoS₂-based photodetectors through hybridization with CdS_{0.42}Se_{0.58} nanobelt, *J. Adv. Dielectr.* 13 (6) (2023) 2345004.
- [7] X. Yin, C. Zhang, Y. Guo, Y. Yang, Y. Xing, W. Que, PbS QD-based photodetectors: future-oriented near-infrared detection technology, *J. Mater. Chem. C* 9 (2) (2021) 417–438.
- [8] C. Zhang, X. Yin, G. Chen, Z. Sang, Y. Yang, W. Que, High-performance photodetector with a-IGZO/PbS quantum dots heterojunction, *ACS Photonics* 10 (3) (2023) 790–800.
- [9] M. Liu, N. Yazdani, M. Yarema, M. Jansen, V. Wood, E.H. Sargent, Colloidal quantum dot electronics, *Nat. Electron.* 4 (8) (2021) 548–558.
- [10] S. Jee, M.-J. Si, J.-H. Choi, D. Kim, C. Kim, D. Yang, S.-W. Baek, P-type colloidal InSb quantum dot ink enables III-V group bulk-heterojunction shortwave infrared (SWIR) photodetector, *Adv. Opt. Mater.* 12 (18) (2024) 2303097.
- [11] M.-J. Si, S. Jee, M. Yang, D. Kim, Y. Ahn, S. Lee, C. Kim, I.-H. Bae, S.-W. Baek, Colloidal InAs quantum dot-based infrared optoelectronics enabled by universal dual-ligand passivation, *Adv. Sci.* 11 (13) (2024) 2306798.
- [12] V. Adinolfi, E.H. Sargent, Photovoltage field-effect transistors, *Nature* 545 (7653) (2017) , 252–252.
- [13] G. Konstantatos, I. Howard, A. Fischer, S. Hoogland, J. Clifford, E. Klem, L. Levina, E.H. Sargent, Ultrasensitive solution-cast quantum dot photodetectors, *Nature* 442 (7099) (2006) 180–183.
- [14] J.P. Clifford, G. Konstantatos, K.W. Johnston, S. Hoogland, L. Levina, E.H. Sargent, Fast, sensitive and spectrally tuneable colloidal quantum-dot photodetectors, *Nat. Nanotechnol.* 4 (1) (2009) 40–44.
- [15] C.R. Kagan, E. Lifshitz, E.H. Sargent, D.V. Talapin, Building devices from colloidal quantum dots, *Science* 353 (6302) (2016) aac5523.
- [16] C.-H.M. Chuang, P.R. Brown, V. Bulovic, M.G. Bawendi, Improved performance and stability in quantum dot solar cells through band alignment engineering, *Nat. Mater.* 13 (8) (2014) 796–801.
- [17] S.-W. Baek, S. Jun, B. Kim, A.H. Proppe, O. Ouellette, O. Voznyy, C. Kim, J. Kim, G. Walters, J.H. Song, et al., Efficient hybrid colloidal quantum dot/organic solar cells mediated by near-infrared sensitizing small molecules, *Nat. Energy* 4 (11) (2019) 969–976.
- [18] L. Hu, Z. Zhang, R.J. Patterson, Y. Hu, W. Chen, C. Chen, D. Li, C. Hu, C. Ge, Z. Chen, et al., Achieving high-performance PbS quantum dot solar cells by improving hole extraction through Ag doping, *Nano Energy* 46 (2018) 212–219.
- [19] G.H. Carey, A.L. Abdelhady, Z. Ning, S.M. Thon, O.M. Bakr, E.H. Sargent, Colloidal Quantum Dot Solar Cells, *Chem. Rev.* 115 (23) (2015) 12732–12763.
- [20] X. Yin, P. Chen, M. Que, Y. Xing, W. Que, C. Niu, J. Shao, Highly efficient flexible perovskite solar cells using solution-derived NiO_x hole contacts, *ACS Nano* 10 (3) (2016) 3630–3636.
- [21] Z. Ren, J. Sun, H. Li, P. Mao, Y. Wei, X. Zhong, J. Hu, S. Yang, J. Wang, Bilayer PbS quantum dots for high-performance photodetectors, *Adv. Mater.* 29 (33) (2017) 1702055.
- [22] K. Lu, Y. Wang, Z. Liu, L. Han, G. Shi, H. Fang, J. Chen, X. Ye, S. Chen, F. Yang, et al., High-efficiency PbS quantum-dot solar cells with greatly simplified fabrication processing via "solvent-curing", *Adv. Mater.* 30 (25) (2018) 1707572.
- [23] B.-S. Kim, J. Hong, B. Hou, Y. Cho, J.I. Sohn, S. Cha, J.M. Kim, Inorganic-ligand exchanging time effect in PbS quantum dot solar cell, *Appl. Phys. Lett.* 109 (6) (2016) 063901.
- [24] F. Jiang, W.C.H. Choy, X. Li, D. Zhang, J. Cheng, Post-treatment-free solution-processed non-stoichiometric NiO_x nanoparticles for efficient hole-transport layers of organic optoelectronic devices, *Adv. Mater.* 27 (18) (2015) 2930–2937.
- [25] X. Yin, Y. Guo, H. Xie, W. Que, L.B. Kong, Nickel oxide as efficient hole transport materials for perovskite solar cells, *Sol. Rrl* 3 (5) (2019) 1900001.
- [26] J. Tang, K.W. Kemp, S. Hoogland, K.S. Jeong, H. Liu, L. Levina, M. Furukawa, X. Wang, R. Debnath, D. Cha, et al., Colloidal-quantum-dot photovoltaics using atomic-ligand passivation, *Nat. Mater.* 10 (10) (2011) 765–771.
- [27] C. Zhang, X. Yin, G. Qian, Z. Sang, Y. Yang, W. Que, Gate voltage adjusting PbS-I quantum-dot-sensitized InGaZnO hybrid phototransistor with high-sensitivity, *Adv. Funct. Mater.* 34 (4) (2023) 2308897.
- [28] Y. Yang, Z. Rao, Q. Xu, Y. Liang, L. Yang, Improving the photovoltaic performance for PbS QD thin film solar cells through interface engineering, *J. Colloid Interface Sci.* 627 (2022) 562–568.